Journal

Thermal Conductivity in Nanocrystalline Ceria Thin Films

Marat Khafizov,[‡,†] In-Wook Park,[§] Aleksandr Chernatynskiy,[¶] Lingfeng He,[∥] Jianliang Lin,[§] John J. Moore,[§] David Swank,[‡] Thomas Lillo,[‡] Simon R. Phillpot,[¶] Anter El-Azab,[††] and David H. Hurley[‡]

[‡]Department of Materials Science and Engineering, Idaho National Laboratory, Idaho Falls, Idaho 83415

[§]Department of Metallurgical and Materials Engineering, Colorado School of Mines, Golden, Colorado 80401

[¶]Department of Materials Science and Engineering, University of Florida, Gainesville, Florida 32611

[∥]Department of Engineering Physics, University of Wisconsin, Madison, Wisconsin 53706

[††]Department of Nuclear Engineering, Purdue University, West Lafayette, Indiana 47907

The thermal conductivity of nanocrystalline ceria films grown by unbalanced magnetron sputtering is determined as a function of temperature using laser-based modulated thermoreflectance. The films exhibit significantly reduced conductivity compared with stoichiometric bulk CeO_2. A variety of microstructure imaging techniques including X-ray diffraction, scanning and transmission electron microscopy, X-ray photoelectron analysis, and electron energy loss spectroscopy indicate that the thermal conductivity is influenced by grain boundaries, dislocations, and oxygen vacancies. The temperature dependence of the thermal conductivity is analyzed using an analytical solution of the Boltzmann transport equation. The conclusion of this study is that oxygen vacancies pose a smaller impediment to thermal transport when they segregate along grain boundaries.

I. Introduction

THE ability to control thermal transport in oxides is important to an array of energy harvesting technologies. For example, metal oxides have a large Seeback coefficient at high temperatures and are candidate materials for advanced thermoelectrics. Much effort has been made to boost the thermoelectric conversion efficiency by reducing the thermal conductivity in these materials.[1–4] Another example involves oxide nuclear fuel used in light water reactors. In nuclear fuel, the thermal conductivity is closely related to energy conversion efficiency as well as reactor safety. Understanding the mechanisms that cause a reduction in thermal conductivity in a high radiation environment is important for designing new high-burnup fuels.[5–7] It is well-known that metal oxides are typically electrical insulators in which thermal energy is primarily transported by phonons. In this context, the phonon mean free path is a key parameter that determines thermal conductivity.[8,9]

In perfect single crystals, lattice anharmonicity leads to Umklapp scattering of phonons, which is the primary mechanism that limits thermal transport at high temperatures.[10–12] In materials suitable for practical energy applications, phonon scattering by microstructural features can also play a significant role in limiting thermal transport. For example, in nanocrystalline materials, where the phonon mean free path

is comparable to the grain size, grain boundaries can play an important role in limiting thermal transport.[13–16] In nonstoichiometric and doped oxides, point defects in the form of oxygen vacancies, interstitials, and cation substitutional defects serve to effectively scatter phonons.[17–20] Lastly, dislocations introduced during the fabrication process can also limit the phonon mean free path.[21]

The presence of multiple defect scattering mechanisms makes it hard to isolate and interpret thermal transport data. Thus, many investigators have embarked on separate effects studies. These studies have provided valuable insight into the fundamental mechanisms at play in thermal transport in solids with defects. However, it can be expected that there will also be cooperative effects that cannot be simply understood by adding the contribution of separate defects. For example, in nonstoichiometric oxides, the presence of dislocation and grain boundaries directly impacts the distribution of intrinsic point defects, and in turn, modifies their impact on phonon transport.[22,23] In this study, we measured the thermal transport properties of ceria thin films grown by unbalanced magnetron sputtering. Our major interest is to characterize the interplay between point defects, dislocations, and grain boundaries in limiting thermal transport.

II. Experiment

To understand the combined role of multiple defects, we performed thermal transport measurements on nonstoichiometric nanocrystalline ceria thin films. The films have a columnar grain structure with the column axis oriented parallel to the surface normal. They were deposited onto silicon substrates in an argon–oxygen atmosphere using unbalanced magnetron sputtering.[24,25] Typical deposition conditions are summarized in Table I.

(1) Microstructure Characterization

The crystal structure was analyzed by X-ray diffraction (XRD; PHILIPS, X'Pert-MPD System, Mahwah, NJ) using $CuK\alpha$ radiation. The cross-sectional microstructure and the grain size were characterized using a field-emission scanning electron microscope (FESEM; JSM-7000F, Peabody, MA) operated at a 10 kV. Transmission electron microscopy (TEM) (Philips, EM420, Mahwah, NJ, operating at 120 kV) was used to characterize extended defects. TEM samples of the ceria film were made by dissolving the silicon substrate in a solution of nitric acid—25% hydrofluoric acid. The ceria film was then captured on a copper mesh folding grid and ion milled to electron transparency (GATAN, DuoMill, Model 600TMP, Pleasanton, CA, operating at 6 kV, 1 mA,

---

Table I. Typical Deposition Conditions of CeO$_2$ Films by the Unbalanced Magnetron Sputtering

Deposition parameter	Range of value				
Sample ID	TF#1	TF#2	TF#3	TF#4	TF#5
Target			Ce (99.99%)		
Substrate			Si (100) wafer		
Base pressure (Pa)			~6.7 × 10^{-4}		
Working pressure (Pa)			4.0 × 10^{-1}		
Sputter power (W)			700		
Amount of O$_2$ in atmosphere (%)	40	20	40	40	40
Substrate to target distance (cm)	6.4	7.6	7.6	7.6	6.4
Deposition temperature (°C)	200	400	300	200	400
Deposition time (h)	2	6	6	6	6
Film thickness (μm)	3.7	11.6	11.3	12.5	4.7
Grain size (μm)	0.1	0.3	0.35	0.45	0.5
Thermal conductivity [W (m·K)$^{-1}$]	2.9 ± 0.4	6.8 ± 0.2	6.8 ± 0.2	7.2 ± 0.6	7.3 ± 0.1

with a 20° milling angle). X-ray photoelectron spectroscopy (XPS; PHI XPS Systems, 5600LS, Chanhassen, MN) utilizing a monochromatic Al source was used to observe the chemical bonding characteristics. The bulk chemical composition of the ceria thin film was measured with an electron probe micro analyzer (EPMA; SHIMADZU EPMA-1600, Kyoto, Japan) using Cr and TiN calibration standards.

The chemical composition of a typical grain boundary was studied using scanning transmission electron microscopy (STEM) and electron energy loss spectroscopy (EELS). This portion of the characterization was conducted on a FEI Titan STEM (Hillsboro, OR) with CEOS probe aberration corrector (Corrected Electron Optical Systems GmbH, Heidelberg, Germany) operated at 200 kV. The EELS spectrum images were taken in EFSTEM mode with 24.5 mrad convergence angle, 52 mrad collection angle and 0.8 eV energy resolution. STEM samples were prepared by a focused ion beam (FIB) FESEM. TEM lamellae were created by coarse trenching 20 μm × 15 μm × 1 μm samples using the FIB. The samples were then welded to a copper TEM grid for final TEM thinning. The samples were thinned to a final thickness of roughly 100 nm using 30 kV. Final cleaning of the sample was conducted using 5 kV.

(2) Thermal Transport Measurements

To investigate intrinsic thermal conductivity dominated by Umklapp scattering processes, thermal transport measurements were performed on a large grained, stoichiometric CeO$_2$ polycrystalline pellet (99.9% AlfaAesar, Ward Hill, MA). The average grain size for this sample is $d = 5$ μm and is much larger than the phonon mean free path at moderate to high temperatures. As a consequence, the primary scattering mechanism is due to three-phonon processes mediated by lattice anharmonicity. The density was measured using Archimedes principle, from which porosity was estimated to be $p = 5\%$. High-temperature thermal diffusivity of ceria was measured on a carbon-coated CeO$_2$ pellet using laser flash apparatus (Netsch LFA 457 MicroFlash, Burlington, MA).

Low-temperature thermal transport properties of both samples were measured using modulated thermoreflectance microscopy (MTRM).[26–28] This measurement technique is well suited to measure thermal transport properties in the lateral direction of the thin film samples, i.e., across the columnar grain boundaries. MTRM, which has been described in detail previously,[29] uses an amplitude-modulated laser to excite thermal waves in the sample. A second laser is used to monitor small temperature-induced changes in reflectivity. The amplitude and phase of the change in reflectivity is recorded using lock-in detection. The phase profile is typically used for analysis because the phase is less susceptible to spatial variations in the sample's unperturbed optical reflec-

tivity. The excitation and detection lasers are focused onto the sample using a single microscope objective (typical spot size at the sample surface is ~2 μm). The thermal properties of the film are extracted by comparing experimental results to a continuum-based heat conduction model.[29] For the MTRM measurements, a thin aluminum metal film is thermally evaporated on top of the samples to ensure strong optical absorption. To isolate defect scattering from Umklapp scattering, experiments were performed at low temperatures.[8,10] For these measurements, the sample was mounted inside a liquid nitrogen cooled cryostat specially designed for optical microscopy. This configuration enables laser-based thermal transport measurements to be made in the temperature range between 77 and 400 K.

III. Results

This section is conveniently divided into two subsections—one regarding sample microstructure and the other concerning thermal transport. Unless otherwise stated, the thin film results are presented for a single representative sample (TF# 4).
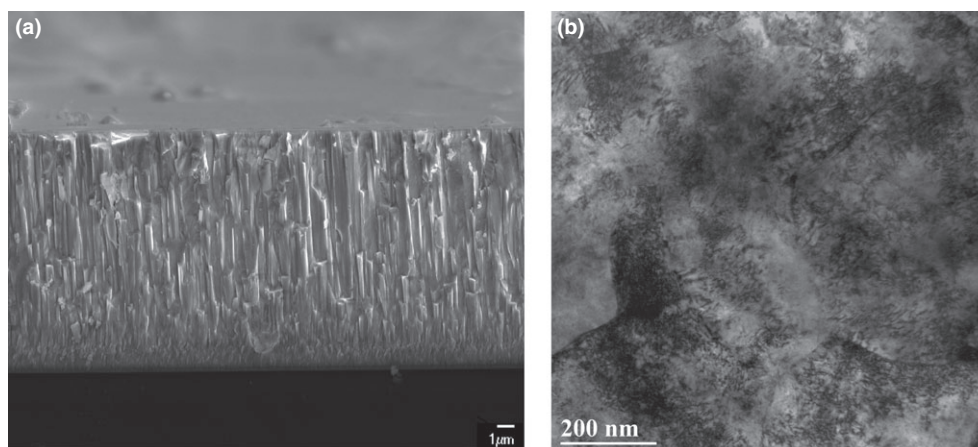
(1) Microstructure

Figure 1(a) shows the XRD pattern for the film sample. The diffraction pattern corresponds to a face centered cubic structure grown along the [111] direction. Careful analysis of XRD peaks associated with diffraction from [111] plane [inset of Fig. 1(a)] suggests a larger lattice constant for the film sample compared to the stoichiometric pellet sample. No reflections corresponding to crystalline Ce$_2$O$_3$ are observed. The Ce 3D spectrum as measured by XPS is shown in Fig. 1(b). The Ce 3D spectrum suggests the existence of two species at the surface of the ceria film. The peaks at 879.3, 895.2, and 913.7 eV indicate the presence of Ce^{4+} and the peaks at 886 and 904.5 eV indicates the presence of Ce^{3+} ions. The EPMA characterization of this sample reveals a O/Ce ratio of 0.58. On the basis of the XRD, XPS, and EPMA results, we conclude that thin film is nonstoichiometric (CeO$_{2-x}$ with $x = 0.27$[30]) and has a cubic crystalline structure. This observation is consistent with previous work demonstrating that partially oxygen reduced CeO$_{2-x}$ is stable in the cubic structure up to $x = 0.4$.[31] Our microstructure characterization does not reveal the presence of other impurities above 0.1%.

A SEM micrograph of the thin film sample, shown in Fig. 2(a), reveals a long columnar grain structure with an average column radius ~450 nm. The film thickness of the film is ~12 μm. The film exhibited a reduced grain size in a small region near the substrate–film interface where nucleation occurs. It is typical for columnar-grained films grown in this fashion to exhibit porosity in this region. However, as will be discussed in the next section, our thermal transport
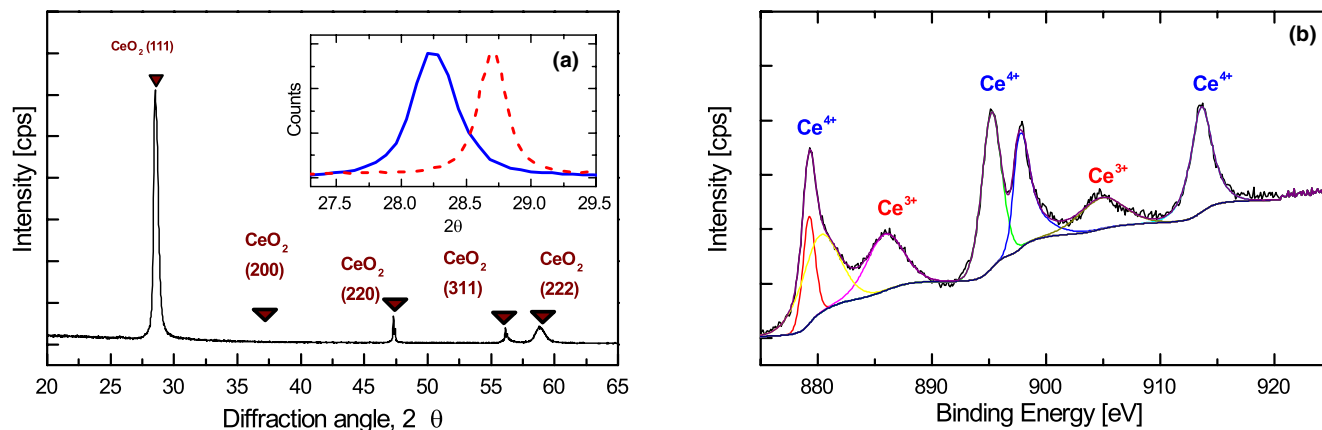
Fig. 1. (a) X-ray diffraction pattern and (b) X-ray photoelectron spectroscopy spectrum of Ce 4*d* for nanocrystalline ceria thin film (TF#4) deposited on Si substrates. Inset in (a) show CeO_2 (111) peaks for thin film (solid line) and pellet (dashed line).

Fig. 2. (a) Columnar grain structure in ceria thin films reveled by a cross-sectional SEM micrograph and (b) plan view TEM image showing a heavily dislocated structure within the ceria grains.

measurements are designed to be minimally affected by the thermal properties of this region. A TEM micrograph of the film sample shown in Fig. 2(b) reveals a high density of dislocation lines. The dislocation density is too high to be accurately determined by TEM, but appears to be comparable to a heavily cold worked metallic alloy which is generally on the order of 10^{16} m^{-2} or greater. These line defects, most likely generated by energetic ion bombardment, do not have enough time to be annealed out during the nonequilibrium magnetron sputtering process.[32]

Figure 3(a) shows the STEM image of a grain boundary in the thin film. The white rectangular zone across the grain boundary was chosen for EELS measurement. Figure 3(b) shows a single Ce $M_{4,5}$-edge EELS spectrum taken from the grain-boundary region and two spectra taken from the grain interior regions in the upper and lower grains. To investigate the valence state of Ce quantitatively, M_5/M_4 intensity ratios across the grain boundary were calculated using the positive part of second derivative of the experimental spectra and plotted in Fig. 3(c). The data presented in this fashion illustrate that there is segregation of Ce^{3+} at the grain boundary.

(2) Thermal Transport

To understand the contribution from three-phonon processes, the thermal diffusivity D of the coarse-grained CeO_2 pellet (average grain diameter is 5 μm) was measured using laser flash from room temperature up to 1000 K and is shown in Fig. 4(a). The thermal conductivity of pellet was determined from $\kappa_p = \rho C D$, where $\rho = 7216$ kg/m^3 is mass density. The temperature-dependent specific heat C was inde-

pendently measured using a calorimeter and was found to agree with the literature values.[33] As the measured conductivity is modified by porosity, we used a modified Loeb expression[17,34] $\kappa_p = \kappa_0 \left[1 - \left(2.6 - 5 \times 10^{-5}(T - 273)p \right) \right]$ to determine the bulk conductivity corresponding to a 100% dense sample. The behavior of the pellet conductivity with temperature is plotted in Fig. 4(b). The $1/T$ temperature dependence is characteristic of phonon-mediated thermal transport limited by Umklapp scattering.

Next, we present thermal transport measurement results for the nanocrystalline ceria thin film. Typical thermal wave phase profiles at room temperature for various modulation frequencies are shown in Fig. 5(a). At high modulation frequencies (100 kHz, circles), the thermal wave is mostly confined to the metal layer, thus it is sensitive to the metal film thermal conductivity. At intermediate frequencies (10 kHz, diamonds) the thermal wave extends into the ceria film, and at low frequencies (1 kHz, squares) the thermal wave extends into the Si substrate.

Determination of thermal conductivity involves fitting a continuum-based model of heat diffusion to the experimental results.[29] The temperature-dependent specific heat and mass density were taken from the literature.[11,35,36] Correction to the specific heat due to a departure from stoichiometry was neglected. For this specific film sample, this analysis gives $\kappa_c = 7.2$ W (m·K)$^{-1}$ at room temperature.

We have performed similar measurements on the other film samples and the results are summarized in Table I. As the grain size increases, the thermal conductivity of the films increases from 2.9 to 7.3 W (m·K)$^{-1}$. It is noted that for all the film samples, the conductivity is noticeably lower than in
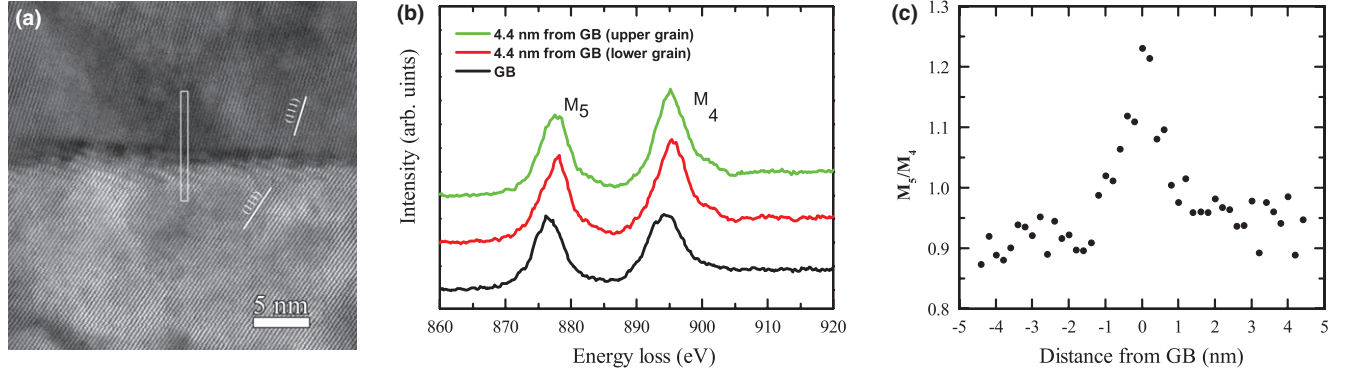
Fig. 3. (a) Scanning transmission electron microscopy image of grain boundary in thin film sample, (b) representative EELS spectra around the Ce $M_{4,5}$—edge, and (c) variation in M_5/M_4 along the line across grain-boundary highlighted area in (a).
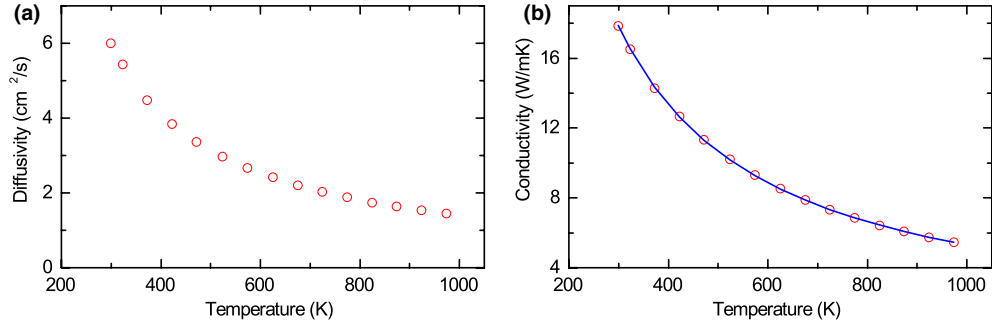
Fig. 4. (a) Thermal diffusivity of CeO_2 pellet measured using laser flash apparatus and (b) corresponding thermal conductivity, where $1/T$—type curve plotted as a guide to the eye.

the ceria pellet ($\kappa_p = 17.5$ W (m·K)$^{-1}$). Figure 5(b) plots the inverse conductivity versus inverse grain size and as discussed later this will be used to extract the grain-boundary resistance. The strong dependence of the thermal conductivity on grain size emphasizes the role of grain boundaries in limiting thermal transport. The influence exerted by the grain boundaries is noteworthy because the phonon mean free path is generally much smaller than the grain sizes investigated.

To further investigate the influence of the grain boundaries, we have performed MTRM experiments on the pellet and film samples at low temperatures. Low-temperature measurements effectively freeze out three-phonon processes allowing other scattering mechanisms to be investigated in detail. Experimental results for the thin film sample and for the pellet are shown in Fig. 6. The thermal conductivity of the pellet increases with a $1/T$ dependence with decreasing temperature. In contrast, the thermal conductivity of the thin film sample is almost constant in the temperature range 150 K < T < 300 K, and gradually decrease for temperatures below 150 K. This behavior, indicative of strong grain-boundary scattering, is similar to that found in previous studies conducted on thin film samples.[15,16,37]

IV. Theoretical Procedure

In this section, we present an analytical model to estimate thermal conductivity taking into account phonon–phonon interactions and defect scattering. Defects are classified within the Boltzmann transport formalism as follows: (1) Point defects have an associated length scale that is much smaller than the dominant phonon wavelength. Point defects include impurities and defects associated with nonstoichiometry. (2) Higher dimensional defects include planar defects such as grain boundaries and line defects such as dislocations. Our estimate of bulk thermal conductivity utilizes a simple analytical solution of the Boltzmann transport equation (BTE) under the relaxation time approximation using

the Debye dispersion relation.[10] In this model, generally referred to as Klemens–Callaway method (KCM), the conductivity is given by the following equation:

$$\kappa_0(T) = \frac{k_B}{2\pi^2 v} \int_0^{\omega_D} \frac{C(T,\omega)\omega^2 d\omega}{\tau^{-1}(T,\omega)} \quad (1)$$

where k_B is Boltzmann constant, v is the sound velocity, ω is the phonon frequency, and ω_D the Debye frequency. The effective sound velocity has been estimated as $v = (1/3v_L^3 + 2/3v_T^3)^{-1/3}$, where v_L and v_T are the longitudinal and transverse sound velocities obtained from the elastic stiffness tensor components C_{11} and C_{44}, $v_L = \sqrt{C_{11}/\rho}$ and $v_T = \sqrt{C_{44}/\rho}$. The Debye frequency, $\omega_D = 53.9$ THz, is calculated based on $\omega_D = v(6N\pi^2/V_0)^{1/3}$, where $V_0 = a^3/4$ is the volume per unit cell, a is the lattice constant, and N is the number of atoms per unit cell. The input parameters needed for the models were calculated based on experimentally measured parameters (Table II) and are summarized in Table III. The specific heat is given by the following equation:

$$C(T,\omega) = \frac{\hbar^2\omega^2 e^{\hbar\omega/k_B T}}{k_B^2 T^2 (e^{\hbar\omega/k_B T} - 1)^2} \quad (2)$$

where T is temperature, $\hbar$ Plank's constant.

The scattering rate τ^{-1} is combination of different scattering processes and is given by the following equation[10]:

$$\tau^{-1}(T,\omega) = A\omega^4 + B\exp\left(-\frac{T_D}{3T}\right)\omega^2 T + \frac{v}{L} \quad (3)$$

where $T_D = \hbar\omega_D/k_B$ is Debye temperature. The first term in this expression takes into account the contribution from isolated point defects, the second term describes phonon–phonon interactions at temperatures below the Debye
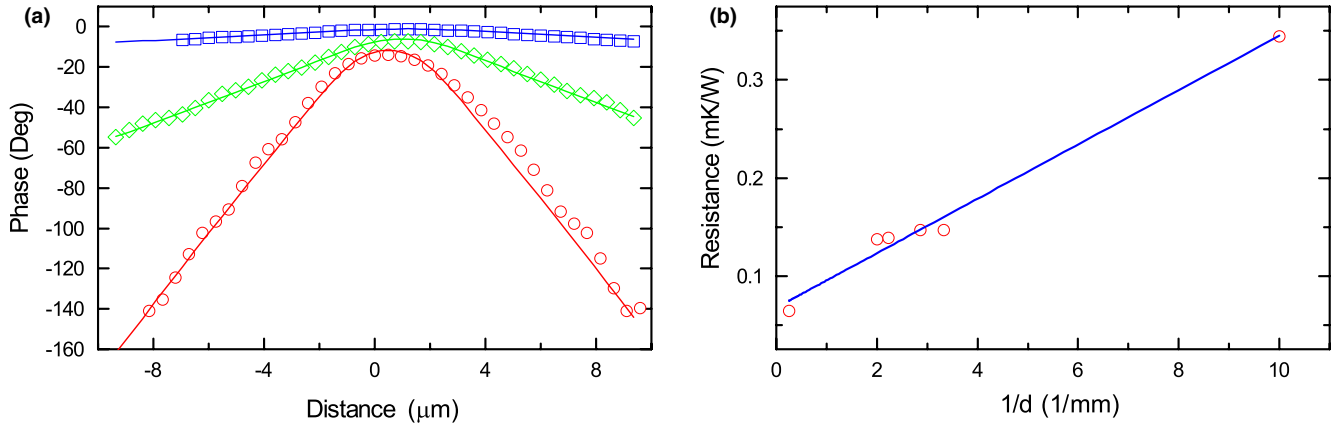
Fig. 5. (a) Thermal wave profile in ceria thin film (TF#4) at 1 kHz (square), 10 kHz (diamond), and 100 kHz (circles) modulation frequencies, solid lines are fits to the continuum-based thermal heat diffusion model. Phase is plotted as a function of probe scan distance, where pump is located at the origin (b) Dependence of thermal conductivity on grain size at room temperature measured using modulated thermoreflectance microscopy.

temperature and the last term represents sample boundary scattering with L being the size of the sample. The parameter A depends on the difference in mass and difference in radius between substitutional and host atoms[38–40]:

$$A = \frac{V_0}{4\pi N \upsilon^3} \sum \Gamma_i$$
$$= \frac{V_0}{4\pi N \upsilon^3} \sum f_i \left[\left(\frac{M_i - M_a}{M_a} \right)^2 + \varepsilon \left(\frac{r_i - r_a}{r_a} \right)^2 \right] \quad (4)$$

where M_i and r_i are the mass and ionic radius of the ith atom, M_a and r_a are the mean mass and ionic radius of the structure, respectively, ε is parameter representing the magnitude of the strain field associated with ion radius mismatch, and f_i is the atomic fraction of atom i. The coefficient B is related to the cumulative contribution from all allowed three-phonon processes. Boundary scattering from the external boundaries of the sample has a negligible contribution at the temperatures investigated.

Various approaches have been developed to account for grain-boundary scattering within the KCM model. While the KCM has been applied to polycrystals by adding a boundary scattering relaxation time[41,42] into the total relaxation time, the thermal conductivity can be calculated as a function of average grain size only after including a number of adjustable parameters. It is therefore more natural to consider an effective medium approach that addresses more directly the fundamental role of the boundary. This approach was first developed by Nan and Birringer.[43] For polycrystals with isotropic spherical crystallites, the thermal conductivity can be written in terms of the average Kapitza conductance, σ, and the average grain size, d as follows:

$$\frac{1}{\kappa} = \frac{1}{\kappa_0} + \frac{1}{\sigma d} \quad (5)$$

where the bulk conductivity, κ_0, is given by Eq. (1). The temperature dependence of σ can be expressed by the following equation[27]:

$$\sigma(T) = \frac{k_B}{2\pi^2 \upsilon^2} \int_0^{\omega_D} C(T, \omega) \alpha(\omega) \omega^2 d\omega \quad (6)$$

where $\alpha(\omega)$ is the frequency dependent transmission coefficient.

Finally, dislocations influence the thermal conductivity in two ways: via phonon interaction with the extended strain field surrounding the dislocation and via interaction with the dislocation core. The former usually dominates, and can be considered by including an additional term in the expression for the relaxation time via Matthiesen rule[39]:

$$\tau_d^{-1}(\omega) = \frac{2^{3/2}}{3^{7/2}} \mu N_D b^2 \gamma^2 \omega = D\omega \quad (7)$$

In this expression, μ is a coefficient that depends on the angle between the dislocation line and heat current, N_D represents the dislocation density, b is the dislocation Burgers vector, and γ is the Grüneisen parameter. This expression is derived using the same level of approximation as other contributions in the Eq. (3). For dislocations having a random orientation distribution, $\mu = 0.55$ and b is on the order of the lattice constant.

V. Discussion

In the remainder of this manuscript, we present discussion on the possible mechanisms limiting thermal conductivity in the ceria films. Our goal was to understand the collective influence of the observed microstructural features. First, we analyze the conductivity of the CeO_2 pellet within the KCM framework. It is used as a reference material for anharmonic three-phonon scattering. Then, we apply the KCM to the thin film samples, where we consider the effect of oxygen vacancies, grain boundaries, and dislocation lines. Finally, we use the outcome of this analysis to determine the collective influence of these microstructure features on thermal transport.

The measured thermal conductivity of the pellet over a broad temperature range is presented in Fig. 4(b). It follows a

Table II. Physical Properties of CeO_2 used for Modeling and Calculation of Parameters[55–57]

Physical parameter	Value
Unit cell, a (nm)	0.541
Number of atom per cell, N	3
Density, ρ (kg/m^3)	7216
Elastic constant, C_{11} (GPa)	403
Elastic constant, C_{44} (GPa)	60

Table III. Calculated Physical Properties of CeO_2

| Physical parameter	Value
Sound velocity, υ (m/s)	3270
Debye frequency, ω_D (THz)	53.8
Debye temperature, T_D (K)	409

typical $1/T$ dependence, representative of thermal transport limited by intrinsic three-phonon scattering processes. A best fit of the KCM model to the experimental data is presented in the inset of Fig. 6. Only two parameters were used as fitting parameters. We obtain a value of $A = 44.1 \times 10^{-44}$ s^3, typical value for high purity samples[8,44] and $B = 1.6 \times 10^{-18}$ s/K. Using an expression[11,45] $B = \hbar\gamma^2/M\upsilon T_D$, where M is average mass per atom, $M = \rho V_0/N$, our results suggests $\gamma = 2.5$, a higher value than $\gamma = 1.24$ reported for optical phonon modes in CeO$_2$.[46]

First, we consider the effect of off-stoichiometry on thermal transport in thin film sample by assuming a uniform distribution of oxygen vacancies. Proper treatment requires that for every oxygen vacancy two atoms of cerium need to change their charge states from Ce^{4+} to Ce^{3+} to preserve charge neutrality. There are two approaches available in the literature for calculating Γ for nonstoichiometric samples. The first was introduced by Slack for multicomponent systems[8] and the second was introduced by Gibby[47] and extended by Fukushima *et al.* for actinide bearing solid solutions.[48] We use the Gibby approach as it has been successfully applied to similar systems such as UO$_2$ and mixed U$_{1-y}$M$_y$O$_{2-x}$, where the mass of cation is significantly larger than the anion. Within this framework, the scattering cross section due to point defect scattering is given by the following equation[48]:

$$\Delta\Gamma = \sum_i \left| \Gamma_{i(CeO_{2-x})} - \Gamma_{i(CeO_2)} \right| =$$

$$\left[\frac{1}{3}\left| \frac{M_{Ce}^2}{M_a^2} - \frac{M_{Ce}^2}{M_0^2} \right| + \frac{1}{3}\left| \frac{(2-x)M_O^2}{M_a^2} - \frac{2M_O^2}{M_0^2} \right| + \right.$$
$$\left. + \frac{\varepsilon}{3}\left| \frac{(1-2x)r_{Ce^{4+}}^2 + 2xr_{Ce^{3+}}^2}{r_a^2} - \frac{r_{Ce^{4+}}^2}{r_0^2} \right| + \frac{\varepsilon}{3}\left| \frac{(2-x)r_{O^{2-}}^2 + xr_{O^v}^2}{r_a^2} - \frac{2r_{O^{2-}}^2}{r_0^2} \right| \right] \quad (8)$$

where M_{Ce} and M_O are masses of cerium and oxygen atoms and their corresponding ions, $r_{Ce^{4+}}$, $r_{Ce^{3+}}$, $r_{O^{2-}}$, and r_{O^v} are radia of the Ce^{4+}, Ce^{3+}, O^{2-}, and O^v ions, respectively, and $M_0 = 1/3(M_{Ce} + 2M_O)$, $r_0 = 1/3(r_{Ce^{4+}} + 2r_{O^{2-}})$, $M_a = 1/3(M_{Ce} + (2-x)M_O)$, and $r_a = 1/3((2-x)r_{Ce^{4+}} + 2xr_{Ce^{3+}} + (2-x)r_{O^{2-}} + xr_{O^v})$. The impurity concentration is measured to be less than 0.1%, two orders of magnitude smaller than oxygen vacancy concentration. Therefore, we neglect the influence of impurity scattering in our analysis.

Using the parameters given in Table IV and $\varepsilon = 100$, typical value used for heavy-metal oxides,[48,49] we find that for
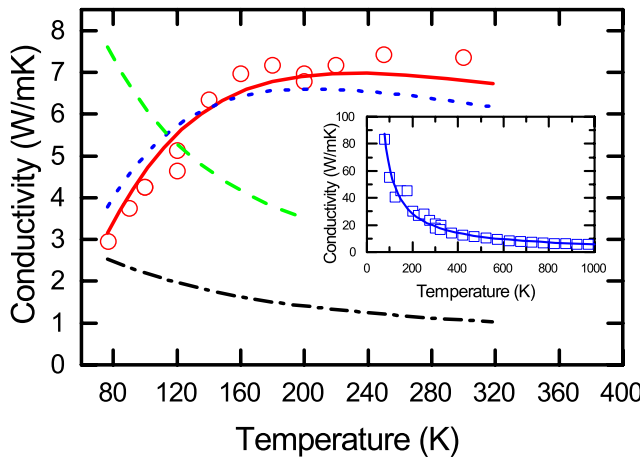
Fig. 6. Low-temperature thermal conductivity of ceria samples measured using thermal wave imaging. (squares—pellet, circles—thin film). Lines are the fit via the Klemens–Callaway model (dashed line —KCM fit with point defects only, solid line—fit with grain boundaries as primary scattering mechanism, dotted line—fit with dislocation line scattering, and dash-dotted line is prediction of KCM assuming uniform distribution of point defects).

$x = 0.27$ the BTE model predicts a substantial reduction in conductivity (dash-dotted line Fig. 6). Our estimate at $T = 300$ K is $\kappa = 1.2$ W (m·K)$^{-1}$, well below measured value and close the lower limit in a strongly disordered crystals $\kappa = 0.9$ W (m·K)$^{-1}$ (i.e., amorphous limit for thermal transport[50]). This result is most likely an indication that the coefficient A given in Eq. (4) is not appropriate for such large excursions from stoichiometry.[49] We are not aware of studies involving the influence of off-stoichiometry on thermal transport in CeO$_{2-x}$; however, in the study of isostructural UO$_{2\pm x}$ using molecular dynamics simulation, Watanabe *et al.*[19] found that for both hypo and hyperstoichiometric systems the lower limit of thermal conductivity is reached for $x = 0.125$. A similar result has been obtained experimentally by Amaya *et al.*[18] Therefore, it is an interesting observation that such highly nonstoichiometry films exhibits conductivity well above amorphous limit.

To further consider the role of large deviations in stoichiometry, we adopt the approach of Amaya *et al.*[18] and treat the coefficient A in Eq. (3) as a fitting parameter (equivalent to using ε as a fitting parameter). The best fit curve, shown as the dashed line in Fig. 6, substantially overestimates the conductivity for temperatures below ~120 K and underestimates the conductivity for temperature above ~120 K. In addition, by considering A and B as fitting parameters in Eq. (4), we obtain an unphysical value for parameter $B = 3.8 \times 10^{-28}$ s/K and a best fit conductivity curve that fails to capture the functional form of temperature dependence (not shown, but similar to dashed line). These observations taken together suggest that point defects acting in isolation cannot account for the observed conductivity data.

Next, consider the effect of grain boundaries on thermal transport. Using the effective medium model given by Eq. (5), the room-temperature Kapitza conductance can be obtained by fitting the data presented in Fig. 5(b). Our best fit value, $\sigma = 0.036$ GW/m^{2}K. The Kapitza conductance associated with grain boundaries in CeO$_2$ has not been previously reported. However, we do find that our measured value of the Kapitza conductance is over an order of magnitude smaller than that of a UO$_2$ polycrystal calculated by Watanabe *et al.*[51]

To further investigate this mechanism, consider the variation in conductivity with temperature presented in Fig. 6. In this case, the temperature dependence of the bulk conductivity as well as the Kapitza conductance must be taken into account. A model based on Eqs. (1)–(3), (5), and (6) is used to calculate thin film conductivity assuming that the coefficient B has the same numerical value as calculated for the pellet, and A and α are used as fitting parameters. A best fit to the data, is obtained for $A = 0$ and $\alpha(\omega) = 6.2 \times 10^{-2}$ and is shown in Fig. 6(b) (solid line). This value for $\alpha(\omega)$ is approximately two orders of magnitude smaller than the transmission coefficient predicted using the diffuse mismatch model, $\alpha(\omega) = 0.5$.[16] While these results suggest a grain-boundary effect that is uncharacteristically large, the functional relation of the film conductivity with grain size [Fig. 5(b)] and with temperature (Fig. 6) is consistent with a grain-boundary scattering mechanism.

To test if this anomalously small conductance is typical for a grain boundary in ceria, we performed molecular

Table IV. Ion Properties used to Calculate Phonon Scattering from Point Defects[58]

	Ion mass	Ion radius (nm)
Ce^{4+}	140.99	0.097
Ce^{3+}	140.99	0.1143
O^{2-}	16	0.1368
O^v	0	0.1367

Table V. Grain-boundary Conductance of Different Grain-boundary Orientation in CeO$_2$ Calculated by Molecular Dynamics

Grain-boundary type	Boundary conductance (GW/m^{2}K)
$\Sigma3$	2.3
$\Sigma11$	2.7
$\Sigma13$	3.3
$\Sigma3$ (UO$_2$ at 800 K)	1.6

Table VI. Summary of Fitting Results

Point defects, A (s^3)	Grain-boundary transmission coefficient, α	Dislocation line scattering coefficient, D	Goodness of fit, χ^2 (normalized)
4.3×10^{-41}	–	–	11.5
0	6.2×10^{-3}	–	1.3
0	–	3.4×10^{-2}	2.4

– indicates that parameter was not considered.

dynamics (MD) simulations using nonequilibrium molecular dynamics (NEMD).[9] The boundaries considered are ideal in the sense that they are not decorated with lattice defects such as oxygen vacancies. In this approach, a simulation cell is partitioned into a number of slices along one of the crystallographic directions. One of the slices is designated as a heat source, whereas another, on the opposite side of the simulation cell is designated as a heat sink. An equal amount of energy is supplied and removed at the source and the sink. After equilibration, the temperature profile is measured and the thermal conductivity is calculated using Fourier's law. A Buckingham interatomic potential as parameterized by Gotte[52] (neglecting the shell contribution) was used in the simulations. This parameterization includes interactions of Ce^{3+} ions with oxygen, which, therefore, makes studies of the off-stoichiometry possible. Thermal conductivity of the pure CeO$_2$ as predicted by this potential is 19 W (m·K)$^{-1}$ at 300 K, slight overestimate of the experimental value of 17.8 W (m·K)$^{-1}$. We consider a few different types of the grain boundaries to get an idea of a typical grain-boundary conductance for ceria. Results of this investigation are presented in the Table V for $\Sigma3$, $\Sigma13$, and $\Sigma11$ grain boundaries. As one can see, all the conductance values are quite high as compared with our experimental results. From this, we conclude that the boundary conductance measured is anomalously small compared with ideal boundaries.

Next, we consider the effect of dislocations lines. The TEM micrograph in Fig. 2(b) suggests a high density of dislocation lines, however, an estimate of the density from this data was not possible. The effect of dislocations lines can be modeled using Eqs. (1)–(3), and (7). Using the value of the parameter B determined for the pellet, a best fit gives $A = 0$ and $D = 3.4 \times 10^{-2}$. The fitted conductivity curve, plotted in Fig. 6(b) (dotted line), agrees well with experiment data. However, this fit suggests a very high concentration of dislocation lines $N_D \sim 9.8 \times 10^{17}$ m^{-2}, much higher than the typical upper limit, 10^{16} m^{-2}, for highly deformed metals.[53,54] The fitted value of A is zero for both cases presented above. While not a physical result this is an indication of the strong influence of dislocations and/or grain boundaries as compared with point defects.

Our fitting results are summarized in Table VI. We find that our film sample has a conductivity which is much higher than expected assuming a uniform distribution of oxygen vacancies. In addition, we find a good fit to the conductivity variation with temperature if we consider the influence of grain boundaries. However, the measured grain-boundary conductance is anomalously low compared with values calculated using an MD simulation of perfect boundaries. A similar observation is obtained for dislocations. In this case, the estimated dislocation density is anomalously high for oxide materials. To investigate whether these findings are a result of underestimating anharmonic effects in nonstoichiometric samples, we repeated our analysis assuming a value of B that is twice the value that was extracted from the pellet sample. In this case, we find the values for α and D are within 10% of those reported in Table VI. Thus, the uncharacteristic values of α and D do not stem from an underestimation of anharmonicity. These observations suggest that the oxygen vacancies

required to accommodate off-stoichiometry are not uniformly distributed, but rather segregate at extended defects.

While it is possible for the oxygen vacancies to segregate at dislocations, the picture involving segregation at grain boundaries is strongly supported by both the microstructure characterization and thermal conductivity analysis. First, the variation in conductivity with grain size is in keeping with a grain boundary scattering mechanism. Second, the best fit to the conductivity versus temperature data is obtained for a model that considers only grain-boundary scattering (see Table VI). Third, the EELS data shows that there is segregation of Ce^{3+} at the grain boundary. This in turn suggests that oxygen vacancies are also segregated at the grain boundary.[23]

A physical interpretation of the influence of vacancy segregation on thermal transport in our ceria films is as follows:

1. The influence posed by grain boundaries that are decorated with oxygen vacancies is dramatically larger than an ideal boundary.
2. Oxygen vacancies themselves pose a smaller impediment to thermal transport if they segregate at grain boundaries:

   - In the vacancy rich atmosphere around the grain boundary there is a reduction in phonon scattering per point defect when the distance between point defect is decreased below the phonon mean free path.
   - There is an increase in the intragrain conductivity due to a corresponding decrease in point defect density.

VI. Conclusions

Thermal transport in nonstoichiometric, nanocrystalline ceria films grown using unbalanced magnetron sputtering was investigated using laser-based modulated thermoreflectance. The films exhibit significantly reduced conductivity compared with stoichiometric bulk CeO$_2$. An analytical solution of the BTE was used to consider the influence of point defects, grain boundaries and dislocations on thermal conductivity. Our modeling results suggest that oxygen vacancies pose a smaller impediment to thermal transport when they segregate along grain boundaries.

References

[1]M. Ohtaki, T. Tsubota, K. Eguchi, and H. Arai, "High-Temperature Thermoelectric Properties of (Zn$_{1−x}$Al$_x$)O," *J. Appl. Phys.*, **79** [3] 1816–8 (1996).
[2]M. Ohtaki, "Recent Aspects of Oxide Thermoelectric Materials for Power Generation From Mid-to-High Temperature Heat Source," *J. Ceram. Soc. Jpn.*, **119** [1395] 770–5 (2011).
[3]I. Terasaki, Y. Sasago, and K. Uchinokura, "Large Thermoelectric Power in NaCo$_2$O$_4$ Single Crystals," *Phys. Rev. B*, **56** [20] 12685–7 (1997).

[4]J. R. Sootsman, H. Kong, C. Uher, J. J. D'Angelo, C. I. Wu, T. P. Hogan, T. Caillat, and M. G. Kanatzidis, "Large Enhancements in the Thermoelectric Power Factor of Bulk PbTe at High Temperature by Synergistic Nanostructuring," *Angew. Chem. Int. Ed.*, **47** [45] 8618–22 (2008).

[5]J. K. Fink, "Thermophysical Properties of Uranium Dioxide," *J. Nucl. Mater.*, **279** [1] 1–18 (2000).

[6]C. Ronchi, "Thermophysical Properties Affecting Safety and Performance of Nuclear Fuel," *High Temp.*, **45** [4] 552–71 (2007).

[7]P. G. Lucuta, H. Matzke, and I. J. Hastings, "A Pragmatic Approach to Modelling Thermal Conductivity of Irradiated UO$_2$ Fuel: Review and Recommendations," *J. Nucl. Mater.*, **232** [2–3] 166–80 (1996).

[8]G. A. Slack, "Thermal Conductivity of MgO, Al$_2$O$_3$, MgAl$_2$O$_4$, and Fe$_3$O$_4$ Crystals From 3 to 300 K," *Phys. Rev.*, **126** [2] 427–41 (1962).

[9]P. K. Schelling and S. R. Phillpot, "Mechanism of Thermal Transport in Zirconia and Yttria-Stabilized Zirconia by Molecular-Dynamics Simulation," *J. Am. Ceram. Soc.*, **84** [12] 2997–3007 (2001).

[10]J. Callaway, "Model for Lattice Thermal Conductivity at Low Temperatures," *Phys. Rev.*, **113** [4] 1046–51 (1959).

[11]C. J. Glassbrenner and G. A. Slack, "Thermal Conductivity of Silicon and Germanium from 3°K to Melting Point," *Phys. Rev.*, **134** [4A] A1058–69 (1964).

[12]P. G. Klemens, "Heat Conduction in Solids by Phonons," *Thermochim. Acta*, **218**, 247–55 (1993).

[13]S. Raghavan, H. Wang, R. B. Dinwiddie, W. D. Porter, and M. J. Mayo, "The Effect of Grain Size, Porosity and Yttria Content on the Thermal Conductivity of Nanocrystalline Zirconia," *Scripta Mater.*, **39** [8] 1119–25 (1998).

[14]T. Watanabe, B. Ni, S. R. Phillpot, P. K. Schelling, and P. Keblinski, "Thermal Conductance Across Grain Boundaries in Diamond From Molecular Dynamics Simulation," *J. Appl. Phys.*, **102** [6] 063503, 7pp (2007).

[15]Y. F. Wang, K. Fujinami, R. Z. Zhang, C. L. Wan, N. Wang, Y. S. Ba, and K. Koumoto, "Interfacial Thermal Resistance and Thermal Conductivity in Nanograined SrTiO$_3$," *Appl. Phys. Exp.*, **3** [3] 031101, 3pp (2010).

[16]Z. J. Wang, J. E. Alaniz, W. Y. Jang, J. E. Garay, and C. Dames, "Thermal Conductivity of Nanocrystalline Silicon: Importance of Grain Size and Frequency-Dependent Mean Free Paths," *Nano Lett.*, **11** [6] 2206–13 (2011).

[17]P. G. Lucuta, H. Matzke, and R. A. Verrall, "Thermal Conductivity of Hyperstoichiometric SIMFUEL," *J. Nucl. Mater.*, **223** [1] 51–60 (1995).

[18]M. Amaya, T. Kubo, and Y. Korei, "Thermal Conductivity Measurements on UO$_{2+x}$ From 300 to 1400 K," *J. Nucl. Sci. Technol.*, **33** [8] 636–40 (1996).

[19]T. Watanabe, S. G. Srivilliputhur, P. K. Schelling, J. S. Tulenko, S. B. Sinnott, and S. R. Phillpot, "Thermal Transport in Off-Stoichiometric Uranium Dioxide by Atomic Level Simulation," *J. Am. Ceram. Soc.*, **92** [4] 850–6 (2009).

[20]F. Yang, X. F. Zhao, and P. Xiao, "The Effects of Temperature and Composition on the Thermal Conductivities of (ZrO$_2$)(1-x)(CeO$_2$)(x) (0.92)(Y$_2$O$_3$) (0.08) (0 <= x <= 1) Solid Solutions," *Acta Mater.*, **60** [3] 914–22 (2012).

[21]J. Zou, D. Kotchetkov, A. A. Balandin, D. I. Florescu, and F. H. Pollak, "Thermal Conductivity of GaN Films: Effects of Impurities and Dislocations," *J. Appl. Phys.*, **92** [5] 2534–9 (2002).

[22]Y. Y. Lei, Y. Ito, N. D. Browning, and T. J. Mazanec, "Segregation Effects at Grain Boundaries in Fluorite-Structured Ceramics," *J. Am. Ceram. Soc.*, **85** [9] 2359–63 (2002).

[23]H. Hojo, T. Mizoguchi, H. Ohta, S. D. Findlay, N. Shibata, T. Yamamoto, and Y. Ikuhara, "Atomic Structure of a CeO$_2$ Grain Boundary: The Role of Oxygen Vacancies," *Nano Lett.*, **10** [11] 4668–72 (2010).

[24]I.-W. Park, J. Lin, J. J. Moore, M. Khafizov, D. Hurley, M. V. Manuel, and T. Allen, "Grain Growth and Mechanical Properties of CeO$_{2-x}$ Films Deposited on Si(100) Substrates by Pulsed dc Magnetron Sputtering," *Surf. Coat. Technol.*, **217** [0] 34–8 (2013).

[25]J. Lin, J. J. Moore, B. Mishta, M. Pinkas, and W. D. Sproul, "Syntheses and Characterization of TiC/a:C Composite Coatings Using Pulsed Closed Field Unbalanced Magnetron Sputtering (P-CFUBMS)," *Thin Solid Films*, **517** [3] 1131–5 (2008).

[26]A. P. Carolyn and L. E. Gary, "Transient Thermoreflectance From Thin Metal Films," *J. Appl. Phys.*, **60** [1] 285–90 (1986).

[27]R. Allan, O. Jon, W. L. Smith, and D. L. Willenborg, "Detection of Thermal Waves Through Optical Reflectance," *Appl. Phys. Lett.*, **46** [11] 1013–5 (1985).

[28]R. J. Stoner and H. J. Maris, "Kapitza Conductance and Heat-Flow Between Solids at Temperatures From 50 to 300 K," *Phys. Rev. B*, **48** [22] 16373–87 (1993).

[29]M. Khafizov and D. H. Hurley, "Measurement of Thermal Transport Using Time-Resolved Thermal Wave Microscopy," *J. Appl. Phys.*, **110** [8] 083525, 7pp (2011).

[30]A. Khare, R. J. Choudhary, K. Bapna, D. M. Phase, and S. P. Sanyal, "Resonance Photoemission Studies of (111) Oriented CeO$_2$ Thin Film Grown on Si (100) Substrate by Pulsed Laser Deposition," *J. Appl. Phys.*, **108** [10] 103712–5 (2010).

[31]N. V. Skorodumova, M. Baudin, and K. Hermansson, "Surface Properties of CeO$_2$ From First Principles," *Phys. Rev. B*, **69** [7] 075401, 8pp (2004).

[32]J. L. Lin, J. J. Moore, B. Mishra, M. Pinkas, W. D. Sproul, and J. A. Rees, "Effect of Asynchronous Pulsing Parameters on the Structure and Properties of CrAlN Films Deposited by Pulsed Closed Field Unbalanced Magnetron Sputtering (P-CFUBMS)," *Surf. Coat. Technol.*, **202** [8] 1418–36 (2008).

[33]E. G. King and A. U. Christensen, "High-Temperature Heat Contents and Entropies of Cerium Dioxide and Columbium Dioxide"; BM-RI-57891960.

[34]A. L. Loeb, "Thermal Conductivity: VIII, a Theory of Thermal Conductivity of Porous Materials," *J. Am. Ceram. Soc.*, **37** [2] 96–9 (1956).

[35]E. F. Westrum Jr. and A. F. Beale Jr., "Heat Capacities and Chemical Thermodynamics of Cerium(III) Fluoride and Cerium (IV) Oxide From 5 to 300 K," *J. Phys. Chem.*, **65** [2] 353–5 (1961).

[36]P. Flubacher, A. J. Leadbetter, and J. A. Morrison, "The Heat Capacity of Pure Silicon and Germanium and Properties of Their Vibrational Frequency Spectra," *Phil. Mag.*, **4** [39] 273–94 (1959).

[37]H. S. Yang, G. R. Bai, L. J. Thompson, and J. A. Eastman, "Interfacial Thermal Resistance in Nanocrystalline Yttria-Stabilized Zirconia," *Acta Mater.*, **50** [9] 2309–17 (2002).

[38]P. G. Klemens, "The Scattering of Low-Frequency Lattice Waves by Static Imperfections," *Proc. Phys. Soc. London, Sect. A*, **68** [12] 1113–28 (1955).

[39]P. G. Klemens, "Thermal Conductivity and Lattice Vibration Modes," *Solid State Phys.*, **7**, 1–98 (1958).

[40]B. Abeles, "Lattice Thermal Conductivity of Disordered Semiconductor Alloys at High Temperatures," *Phys. Rev.*, **131** [5] 1906–11 (1963).

[41]J. E. Graebner, M. E. Reiss, L. Seibles, T. M. Hartnett, R. P. Miller, and C. J. Robinson, "Phonon Scattering in Chemical-Vapor-Deposited Diamond," *Phys. Rev. B*, **50** [6] 3702–13 (1994).

[42]A. D. McConnell, S. Uma, and K. E. Goodson, "Thermal Conductivity of Doped Polysilicon Layers," *J. Microelectromech. Syst.*, **10** [3] 360–9 (2001).

[43]C.-W. Nan and R. Birringer, "Determining the Kapitza Resistance and the Thermal Conductivity of Polycrystals: A Simple Model," *Phys. Rev. B*, **57** [14] 8264–8 (1998).

[44]M. G. Holland, "Phonon Scattering in Semiconductors From Thermal Conductivity Studies," *Phys. Rev.*, **134** [2A] A471–80 (1964).

[45]D. T. Morelli, T. A. Perry, and J. W. Farmer, "Phonon-Scattering in Lightly Neutron-Irradiated Diamond," *Phys. Rev. B*, **47** [1] 131–9 (1993).

[46]J. R. McBride, K. C. Hass, B. D. Poindexter, and W. H. Weber, "Raman and X-Ray Studies of Ce$_{1-x}$Re$_x$O$_{2-y}$, Where Re = La, Pr, Nd, Ee, Gd, and Tb," *J. Appl. Phys.*, **76** [4] 2435–41 (1994).

[47]R. L. Gibby, "Effect of Plutonium Content on Thermal Conductivity of (U, Pu)O$_2$ Solid Solutions," *J. Nucl. Mater.*, **38** [2] 163–77 (1971).

[48]S. Fukushima, T. Ohmichi, A. Maeda, and M. Handa, "Thermal-Conductivity of (Pu$_{1-x}$Nd$_x$)O$_{2-y}$ and (Pu$_{1-x}$Y$_x$)O$_{2-y}$ Solid-Solutions," *J. Nucl. Mater.*, **115** [1] 118–27 (1983).

[49]C. Duriez, J. P. Alessandri, T. Gervais, and Y. Philipponneau, "Thermal Conductivity of Hypostoichiometric low Pu Content (U, Pu)O$_{2-x}$ Mixed Oxide," *J. Nucl. Mater.*, **277** [2–3] 143–58 (2000).

[50]D. G. Cahill, S. K. Watson, and R. O. Pohl, "Lower Limit to the Thermal-Conductivity of Disordered Crystals," *Phys. Rev. B*, **46** [10] 6131–40 (1992).

[51]T. Watanabe, S. B. Sinnott, J. S. Tulenko, R. W. Grimes, P. K. Schelling, and S. R. Phillpot, "Thermal Transport Properties of Uranium Dioxide by Molecular Dynamics Simulations," *J. Nucl. Mater.*, **375** [3] 388–96 (2008).

[52]A. Gotte, D. Spangberg, K. Hermansson, and M. Baudin, "Molecular Dynamics Study of Oxygen Self-Diffusion in Reduced CeO$_2$," *Solid State Ionics*, **178** [25–26] 1421–7 (2007).

[53]H. Hojo, E. Tochigi, T. Mizoguchi, H. Ohta, N. Shibata, B. Feng, and Y. Ikuhara, "Atomic Structure and Strain Field of Threading Dislocations in CeO$_2$ Thin Films on Yttria-Stabilized ZrO$_2$," *Appl. Phys. Lett.*, **98** [15] 153104, 3pp (2011).

[54]D. Yun, B. Ye, A. J. Oaks, W. Chen, M. A. Kirk, J. Rest, A. M. Yacout, and J. F. Stubbins, "Fission gas Transport and its Interactions with Irradiation-Induced Defects in Lanthanum Doped Ceria," *Nucl. Instrum. Methods Phys. Res., Sect. B*, **272**, 239–43 (2012).

[55]M. Mogensen, N. M. Sammes, and G. A. Tompsett, "Physical, Chemical and Electrochemical Properties of Pure and Doped Ceria," *Solid State Ionics*, **129** [1–4] 63–94 (2000).

[56]A. Nakajima, A. Yoshihara, and M. Ishigame, "Defect-Induced Raman-Spectra in Doped CeO$_2$," *Phys. Rev. B*, **50** [18] 13297–307 (1994).

[57]T. Hisashige, Y. Yamamura, and T. Tsuji, "Thermal Expansion and Debye Temperature of Rare Earth-Doped Ceria," *J. Alloy. Compd.*, **408**, 1153–6 (2006).

[58]R. D. Shannon, "Revised Effective Ionic-Radii and Systematics Studies of Interatomic Distances in Halides and Chalcogenides," *Acta Crystallogr., Sect. A*, **32** [SEP1] 751–67 (1976). □